

Atomic-scale observation of a graded polar discontinuity and a localized two-dimensional electron density at an insulating oxide interface

C.-P. Chang,^{1,2} J. G. Lin,¹ H. T. Jeng,³ S.-L. Cheng,^{1,2} W. F. Pong,⁴ Y. C. Shao,⁴ Y. Y. Chin,⁵ H.-J. Lin,⁵ C. W. Chen,² J.-R. Yang,² C. H. Chen,^{1,6} and M.-W. Chu^{1,*}

¹Center for Condensed Matter Sciences, National Taiwan University, Taipei 106, Taiwan

²Department of Materials Science and Engineering, National Taiwan University, Taipei 106, Taiwan

³Institute of Physics, Academia Sinica, Taipei 115, Taiwan

⁴Department of Physics, Tamkang University, Tamsui 251, Taiwan

⁵National Synchrotron Radiation Research Center, Hsinchu 300, Taiwan

⁶Department of Physics, National Taiwan University, Taipei 106, Taiwan

(Received 16 July 2012; revised manuscript received 18 December 2012; published 19 February 2013)

Using atomically resolved electron energy-loss spectroscopy, the atomic-plane-by-atomic-plane, unit-cell-by-unit-cell stoichiometry, and charge characteristics of the oxide interface $(\text{Nd}_{0.35}\text{Sr}_{0.65})\text{MnO}_3/\text{SrTiO}_3$, with a primitive polar discontinuity of $(\text{Nd}_{0.35}\text{Sr}_{0.65}\text{O})^{0.35+}-(\text{TiO}_2)^0$, were thoroughly investigated. $(\text{Nd}_{0.35}\text{Sr}_{0.65})\text{MnO}_3$ is a strongly correlated insulator and the interface was characterized to be insulating. The cell-specific stoichiometric evaluation unveiled an extensive interdiffusion across the interface. The plane-specific charge characterization revealed that the interdiffusion grades the primitive polar discontinuity. Despite the graded polar discontinuity, a charge transfer inversely into $(\text{Nd}_{0.35}\text{Sr}_{0.65})\text{MnO}_3$ was firmly resolved with a length scale of ~ 2 nm and a charge density on the order of $\sim 10^{13}/\text{cm}^2$ and is effectively mediated by an asymmetric Ti interdiffusion. The intricate electronic correlations of the interfacial $(\text{Nd}_{0.35}\text{Sr}_{0.65})\text{MnO}_3$ unit cells and the interdiffusion-induced chemical disorder tend to render the charges localized, resulting in a localized two-dimensional electron density and thus the insulating interface, in distinct contrast to the conventional understanding of a vanishing charge density for an insulating interface and the metallic two-dimensional electron gas found at other classical polar-discontinuous interface systems. A potential strain manipulation on the electronic localization of the electron density was also proposed.

DOI: [10.1103/PhysRevB.87.075129](https://doi.org/10.1103/PhysRevB.87.075129)

PACS number(s): 73.40.-c, 68.37.Lp, 79.20.Uv, 68.35.Fx

I. INTRODUCTION

In [001]-oriented interfaces of $\text{La}^{3+}\text{Al}^{3+}\text{O}_3(\text{LAO})/\text{Sr}^{2+}\text{Ti}^{4+}\text{O}_3(\text{STO})$ and $\text{La}^{3+}\text{Ti}^{3+}\text{O}_3(\text{LTO})/\text{STO}$ with a primitive interfacial AO-BO_2 polar discontinuity of $(\text{LaO})^{1+}-(\text{TiO}_2)^0$ (ABO_3 being the general perovskite formula), the seminal exploration of an interfacial conductivity between the two respective perovskite insulators had raised tremendous interest in oxide electronics beyond the semiconductor classics.¹⁻⁴ The atomic-scale or unit-cell-scale probing of the conductive LAO/STO and LTO/STO interfaces has been known to be essential for unveiling the origin for the associated metallic two-dimensional electron gas (2DEG).⁵⁻⁹ It was then found that minimizing the primitive electrostatic imbalance through the charge transfer into STO can be the primary factor for the 2DEG formation, and the mixed-valence charge accommodation of the Ti^{4+} into Ti^{3+} readily plays a central role.^{2,6-8} Interdiffusion and/or electron-donor oxygen vacancies, however, cannot be completely excluded as plausible contributing factors,^{2,6-14} and a further characterization of the corresponding effective polar discontinuity is essential for microscopically evaluating the significance of all the factors. In principle, such a characterization should simultaneously yield the information of the interfacial chemical stoichiometry and charge feature at the atomic-plane-by-atomic-plane (for both AO and BO_2), unit-cell-by-unit-cell level, which has not been completely resolved experimentally.⁵⁻⁹

In this work, we report on such a characterization of the $(\text{Nd}_{0.35}\text{Sr}_{0.65})\text{MnO}_3(\text{NSMO})/\text{STO}$ interface with the primitively polar-discontinuous $(\text{MnO}_2)^{0.35+}-(\text{Nd}_{0.35}\text{Sr}_{0.65}\text{O})^{0.35+}$

$(\text{TiO}_2)^0-(\text{SrO})^0$ using electron energy-loss spectroscopy (EELS) in an aberration-corrected scanning transmission electron microscope (STEM).¹⁵ The STEM-EELS combination represents the unparalleled technique for tackling the chemical stoichiometry and electronic identity simultaneously at atomic resolution,^{15,16} and NSMO with nominal mixed-valence $\text{Mn}^{3.65+}$ is a well-understood Mott insulator.¹⁷⁻¹⁹ Intriguingly, the primitively polar-discontinuous NSMO/STO interface was found to be insulating and a two-dimensional electron density unambiguously resides in NSMO at odds with the conventional wisdom that an insulating interface should not display residual charges.²⁰ The length scale and charge density^{21,22} of this two-dimensional electron density were unraveled by the plane-specific, cell-specific STEM-EELS characterizations, and the electronic localization of the electron density was discussed.

II. EXPERIMENTAL

The [001]-oriented NSMO films with a thickness of ~ 20 nm were grown on TiO_2 -terminated STO substrates using pulsed laser deposition with a laser fluence of ~ 1 J/cm² and a repetition rate of 3 Hz. Prior to growths, the substrates were subjected to 1 h of *in situ* cleaning at a substrate temperature of 800 °C and a flowing oxygen ambience with a partial pressure of 10^{-1} Torr. The same substrate temperature and oxygen partial pressure were maintained during the growths. The grown heterostructures were then subjected to *in situ* postannealing at 400 °C with an oxygen partial pressure of

760 Torr for 1 h to fill in oxygen vacancies possibly formed during the growths.⁶ The temperature-dependent resistivity (ρ) characterizations were performed using the standard four-point probe method with a typical specimen dimension of $10 \times 2.5 \text{ mm}^2$. The controlled experiments with two electrodes attached to two opposite edges of the samples, facilitating a current flow through the interface, did not show remarkable differences to the four-point probe measurements performed on the NSMO surface. The transport characteristics shown in the work represent the four-point probe results. The work

function $\sim 4.6 \text{ eV}$ of the NSMO film was estimated using a Kelvin probe, calibrated to the known work function of Au ($\sim 5.1 \text{ eV}$), and the measured work function has important consequences later in the work.

The STEM-EELS specimen preparation has been published elsewhere¹⁶ and the spectroscopic characterizations were performed at room temperature on a JEOL-2100F microscope, operated at 200 keV and equipped with a probe corrector. A STEM-probe convergent semiangle (α) of $\sim 20 \text{ mrad}$ and an EELS collection semiangle (β) of $\sim 30 \text{ mrad}$ were

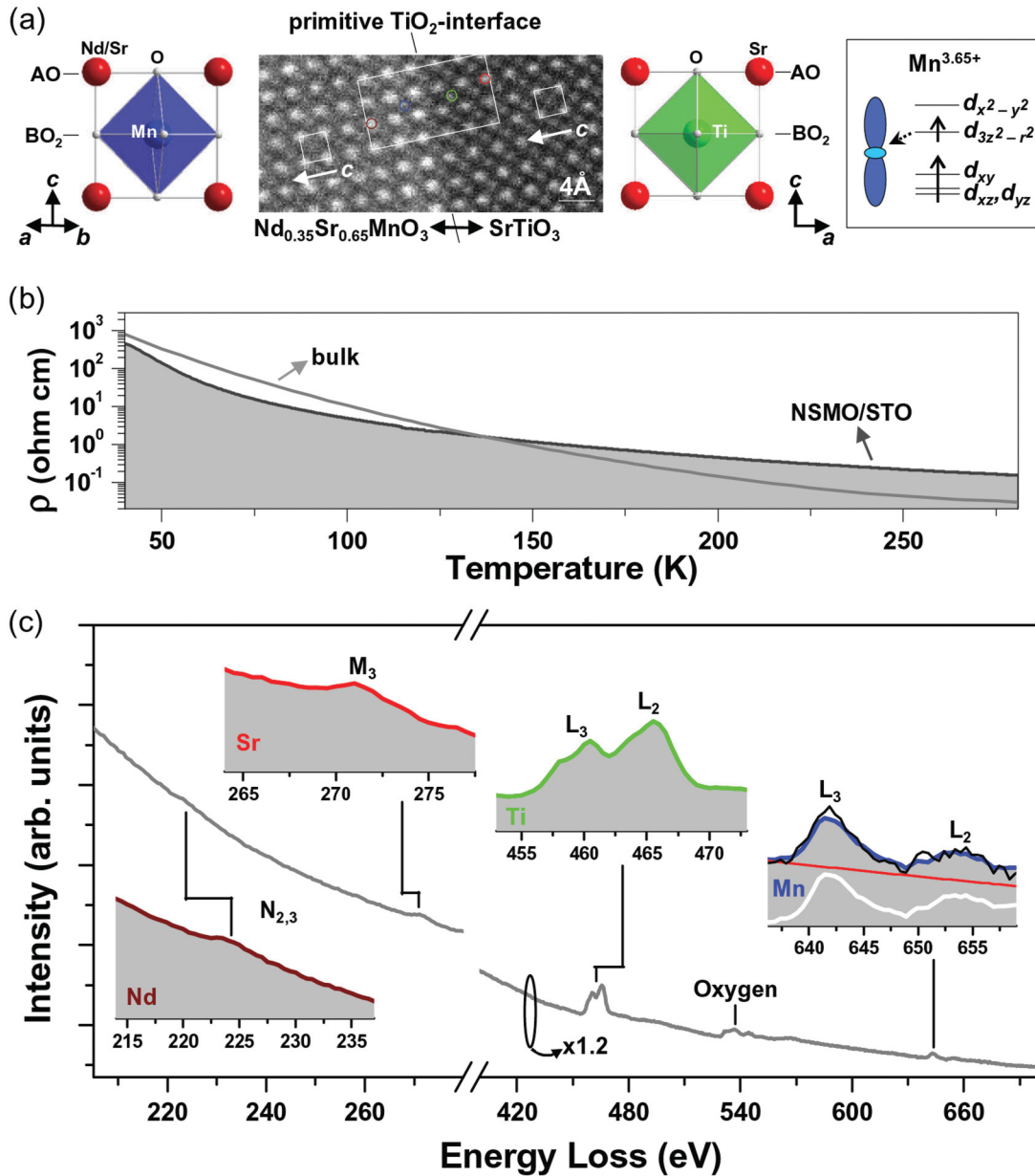


FIG. 1. (Color online) (a) The STEM-HAADF image of *c*-oriented NSMO/STO heterostructure and the schemes of NSMO and STO in the corresponding projections, revealing the respective AO and BO₂ planes. (Right) Boxed scheme shows the nominal *c*-oriented $d_{3z^2-r^2}$ -type orbital of NSMO and the corresponding high-spin state. (b) The resistivity (ρ) of the reference NSMO polycrystalline bulk and the heterostructure. (c) The interfacial STEM-EELS spectra integrated over the rectangle in (a). Insets show the element-specific closeups (PCA processed) of the respective atomic columns in (a), colored circles. The black (blue) curve in Mn- $L_{2,3}$ represents the original (PCA-processed) spectrum, unveiling the spectral-quality improvement by PCA without artifacts. The red (white) curve manifests the background (background-subtracted spectrum).

used, satisfying the incoherent spectral-imaging condition of $\beta > \alpha$, which is essential for achieving atomically resolved STEM-EELS investigations.^{15,16} The corresponding high-angle annular dark-field (HAADF) imaging was acquired with the inner and outer collection semiangles of ~ 190 and ~ 510 mrad, respectively. Within this annular range, no Bragg reflections appear on the imaging detector. Throughout the work, the STEM-probe size (current) of ~ 1.2 Å (~ 120 pA) was exploited and the EELS spectrometer was binned by 20 along the nondispersion direction to improve the readout speed. All STEM-EELS results reported herein were subject to careful principal component analysis (PCA) for removing the spectral random noises.

III. RESULTS AND DISCUSSION

Figure 1(a) shows a STEM-HAADF image of the [001]-oriented NSMO/STO heterostructure, and the abrupt and well-resolved TiO₂-plane interface of the designated (MnO₂)^{0.35-}-(Nd_{0.35}Sr_{0.65}O)^{0.35+}-(TiO₂)⁰-(SrO)⁰ exemplifies a well-controlled film growth. The specimen thickness along the incident electron-probe direction is ~ 30 nm, and the NSMO and STO unit cells are indicated as the respective left and right squares [Fig. 1(a); see also the respective structural schemes]. In our extensive HAADF studies, typical contrasts free from misfit dislocations such as Fig. 1(a) were always observed, suggesting a coherent interface with the tetragonal

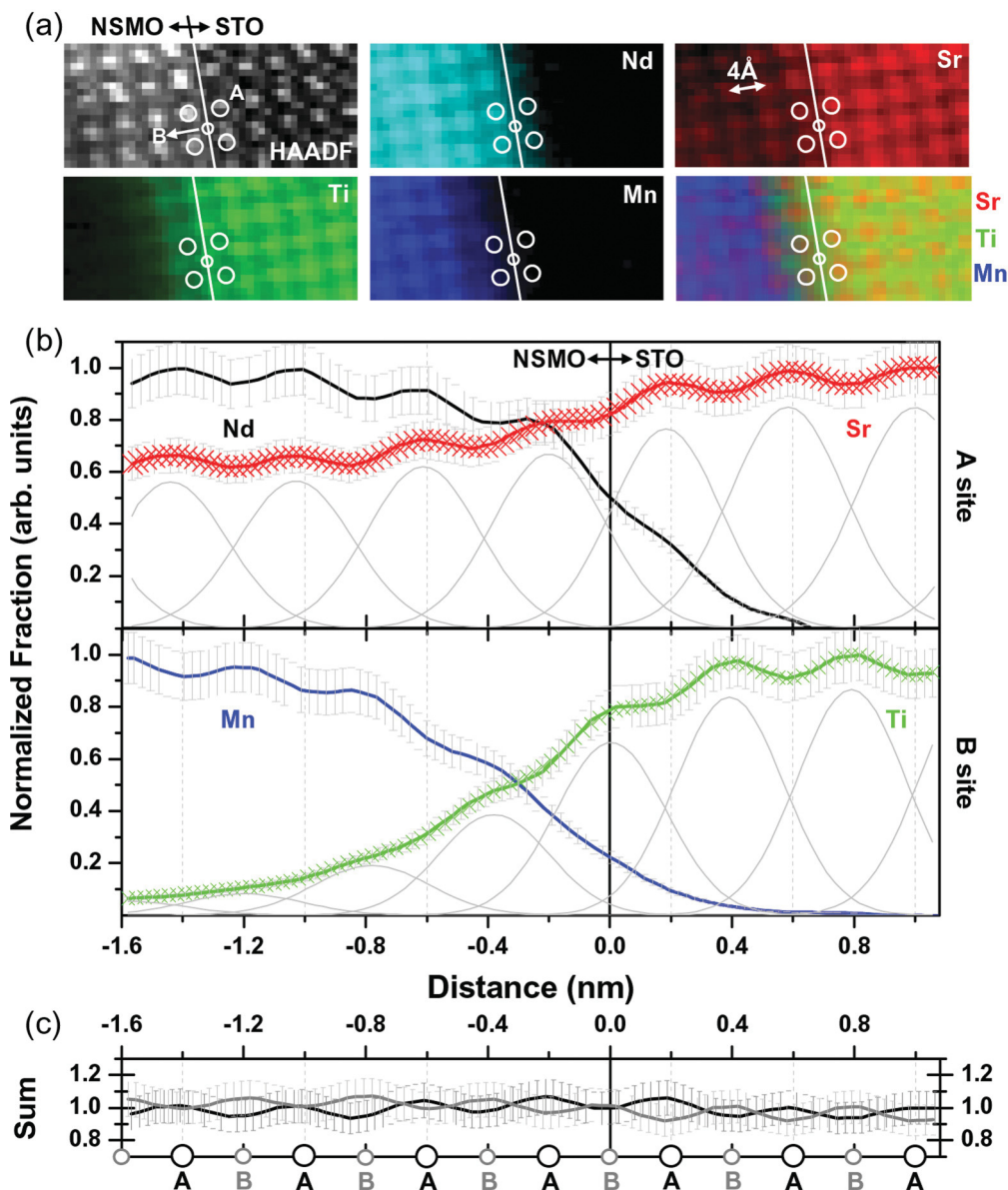


FIG. 2. (Color online) (a) The element-specific maps and corresponding HAADF image; bottom right, the Sr-Ti-Mn overlay. (b) The atomic-plane-by-atomic-plane integrations over (a) and the other four sets of maps, revealing the A- and B-site profiles across the interface. Vertical dashed gray lines are the unit-cell boundaries (for convenience, 4 Å). Gray Gaussians are fits to the respective Sr and Ti positions. Red and green crosses are the Gaussian-fitted profiles. The data in (b) were interpolated for improved Gaussian fits and the ~ 0.7 -Å (one pixel) deviation of some peaks from the unit-cell boundary/center signifies the tolerable mechanical instability upon probing. Vertical bars are estimated statistics errors of, at most, 10%. (c) The AO-plane (black) and BO₂-plane (gray) sums over (b).

NSMO (nominally in-plane constant $a/\sqrt{2}$ of ~ 3.797 Å, Refs. 17–19) elastically accommodating the $\sim 2.7\%$ -tensile strain on STO (unit cell, 3.905 Å). With this noticeable interface quality [Fig. 1(a)], the transport measurement of the heterostructure, however, revealed an insulating feature like that of the well-known bulk reference [Fig. 1(b)]^{17–19} with the absence of a metallic character expected for a primitively polar-discontinuous interface.^{1,2} An insulating character was also revealed in the 5-nm NSMO/STO specimen with a comparable interface quality upon the STEM-HAADF observations. It is then intuitive to envision that a graded polar discontinuity might have taken place, frustrating the interfacial charge transfer^{6,23} and thus resulting in an insulating interface due to the lack of charge carriers therein in accordance with the classical electrostatics.²⁰ To tackle this essential question for the insulating NSMO/STO, an atomic-scale examination of stoichiometric and electronic configurations across the interface is necessary and STEM-EELS represents the ultimate approach.¹⁵ Figure 1(c) shows the Nd-, Sr-, Ti-, and Mn-specific EELS portions (insets) acquired at the individual atomic columns in Fig. 1(a) (individual colored circles; 1-pixel spectra, pixel ~ 0.7 Å) with the pixel dwell time of 100 ms and the spectrometer dispersion of 0.5 eV/channel (thus an energy resolution of ~ 2.5 eV). The same experimental condition was exploited for Fig. 2. The STEM-EELS spectrum [gray

curve, Fig. 1(c)] integrated over the rectangle in Fig. 1(a) is also shown. In effect, the spectral intensity upon each individual atomic column should be linearly proportional to the number of the given atom therein.¹⁵ Further element-specific estimations of the column-by-column spectral intensities could lead to a microscopic evaluation of the local stoichiometry of the interfacial NSMO and STO unit cells upon the achievement of a local, atomic-scale STEM-EELS probing.¹⁵

Figure 2(a) shows the associated chemical maps across the NSMO/STO interface achieved by integrating the respective spectral intensities centered on the carefully obtained background-removed Nd- $N_{2,3}$ and Sr- M_3 (Ti- L_2 and Mn- L_3) maxima through a 4-eV (1-eV) integration window. It is to be mentioned that integrations over the whole $L_{2,3}$ spectral range to generate the Ti and Mn maps did not seem to improve the observed contrasts, which were instead susceptible for background-removal related errors¹⁵ and thus not exploited. No contrast modification to the maps had been performed afterwards. In reference to the *A* and *B* sites resolved in the corresponding HAADF image [Fig. 2(a)], the local contrast maxima within each map are nicely located at the given *A* (Nd, Sr) or *B* (Ti, Mn) sites indicated by the associated white circles, establishing an atomically resolved probing.^{15,16} The mapped contrasts in Fig. 2(a) thus signify the

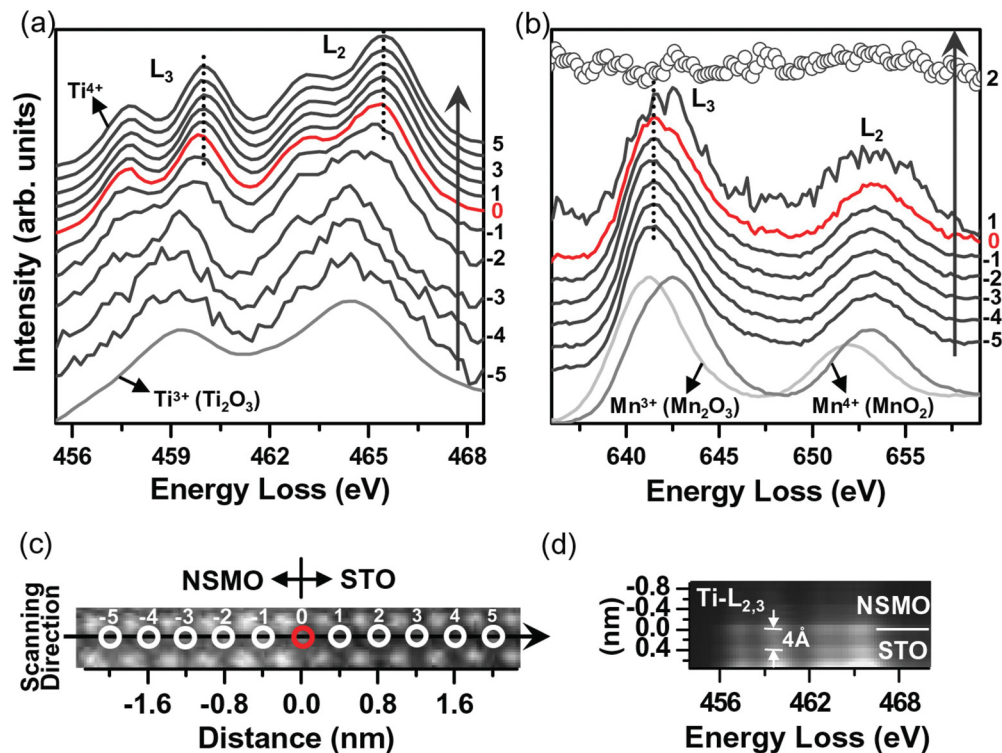


FIG. 3. (Color online) (a) Ti- $L_{2,3}$ and (b) Mn- $L_{2,3}$ spectra of each *B*-site column in (c), circles, upon scanning along the sites (black arrows show the scanning direction). Each spectrum in (a) and (b) represents a spectral-intensity integration of the three pixels (~ 0.7 Å/pixel) centered on the given *B* column in (c), then averaged over three separate experiments to further improve the spectral statistics. The noisy Ti- $L_{2,3}$ spectra from -5 to -3 , (a), result from the finite Ti into NSMO, $\leq \sim 10\%$. The noisy Mn- $L_{2,3}$ in STO, 1 in (b), arises from the same reason. Vanishing Mn features for 3–5 in (b) are like 2, thus are not shown. Dotted lines in (a) and (b) are guides to the eyes for peak-position characterizations. Our fair ~ 1.2 -eV energy resolution herein compromises the primitive line-shape differences between the reference materials (Ti_2O_3 , Mn_2O_3 , and MnO_2) and perovskites. (d) One set out of the three real-space interfacial projections for generating (a). The ~ 4 -Å oscillation, nicely consistently with the *B*-site spacing of also ~ 4 Å, indicates the spatially resolved identity of the spectra.

corresponding compositional profiles,¹⁵ and each element-specific map [Fig. 2(a)], together with the other four sets of maps acquired on different interface regions (~ 20 unit cells in total along the interface), were then integrated for obtaining averaged stoichiometric information of the NSMO/STO interface, as shown in Fig. 2(b) (normalized to the respective NSMO or STO furthest from the interface). To further examine the stoichiometric significance of Fig. 2(b), we summed together the Mn [blue curve, Fig. 2(b)] and Ti (green) profiles for the *B* site and the Nd (black) and Sr (red) profiles for the *A* site upon the renormalization of the Nd curve to a nominal 0.35, and the results are shown in Fig. 2(c). Remarkably, the black AO- and gray BO_2 -plane curves in Fig. 2(c) are complementary to each other with peaks of AO (BO_2) corresponding to valleys of BO_2 (AO), reaffirming the atomic-column resolution exemplified in Fig. 2(a). More importantly, a conservation of the cationic AO- and BO_2 -plane stoichiometry, ~ 1.0 , in ABO_3 perovskites is satisfactorily obtained at the respective *A* and *B* sites [Fig. 2(c)]. This remarkable consistence with the general ABO_3 formula indicates that the AO- and BO_2 -plane peaks in Fig. 2(b) can be utilized for atomic-plane-by-atomic-plane compositional estimations. The cell-specific compositions across the interface can then be derived (Table I), revealing an obvious off-stoichiometry from the nominal NSMO and STO for the interfacial unit cells. Unambiguously, an extensive interdiffusion across the interface occurs and the respective diffusion lengths of Nd, Ti, and Mn can be estimated as the given length scale, below which a clear identification of the corresponding spectral intensity becomes limited by our present chemical-estimation limit of $\sim 3\%$. The diffusion length of Sr was otherwise estimated as the length scale [~ 6 Å, Fig. 2(b)], beyond which the Sr profile in NSMO approaches the nominal ~ 0.65 . While the *A*-site interdiffusion is quite symmetric with the diffusion length of ~ 6 Å for both Nd and Sr [Fig. 2(b)], the *B*-site one is found to be highly asymmetric

[diffusion length ~ 4 Å for Mn, ~ 20 Å for Ti; see also Fig. 3(a) below].

To unveil this distinct asymmetric *B*-site interdiffusion and the potential effect of the overall interdiffusion on the insulating NSMO/STO interface, we examined the charge characteristics of the interfacial Ti and Mn through the respective Ti- and Mn- $L_{2,3}$ spectra [Figs. 3(a) and 3(b)] taken on each individual *B*-site column indicated in Fig. 3(c) (circles) with the pixel dwell time of 800 ms and the spectrometer dispersion of 0.2 eV/channel that improves the energy resolution to ~ 1.2 eV. Each spectrum represents an averaging over three sets of separate experiments, and one set of the interfacial portions is exhibited in Fig. 3(d). Intriguingly, the asymmetric Ti interdiffusion into NSMO [Fig. 3(a)] is accompanied with a gradual valence change from Ti^{4+} (column 5, STO) to Ti^{3+} (column -5 , NSMO) in accordance with the Ti^{3+} -reference spectrum of Ti_2O_3 . The simultaneously acquired Mn- $L_{2,3}$ spectra are, however, monotonous with practically constant line positions and shapes throughout the unit cells [columns -5 to 0, Fig. 3(b)], suggesting that in the presence of the mixed-valence Ti the charge character of $Mn^{3.65+}$ remains electronically stable.²⁴ This latter character will be expounded upon shortly. The vanishing Mn on STO column 1 [$\sim 3\%$, Fig. 2(b)] leads to noisy Mn- $L_{2,3}$ [column 1, Fig. 3(b)] and, for simplicity, the electronic stability of $Mn^{3.65+}$ is presumed on column 1. Figure 4(a) shows the Ti^{3+} fractions and related averaged-Ti valences from columns -5 to 3, derived by linear least-squares fits (triangles) to each spectrum in Fig. 3(a) with the spectra on columns 5/ -5 as the Ti^{4+}/Ti^{3+} reference sets.^{6,25}

Applying then the column-specific valences of the mixed-valence Ti and $Mn^{3.65+}$ [triangles, Figs. 4(a) and 3(b), respectively] and also the nominal charges of Nd^{3+} and Sr^{2+} into the estimated cell-specific compositions in Table I, the unit-cell-by-unit-cell [Fig. 4(b)] and atomic-plane-by-atomic-plane charge characteristics [Fig. 4(c)] are now established.

TABLE I. Cell-by-cell compositions derived from the STEM-EELS composition estimations in Fig. 2(b). The *B*-site sum with a value of slightly larger than unity on the NSMO side in Fig. 2(c) could be associated with the profile normalizations in Fig. 2(b). For convenience of the *B*-site derivations herein, the Ti composition at each individual unit cell was considered as the internal reference for deducing the corresponding Mn one. This approach is tolerable within the estimation limit of our experiments and its influence on the respective cell-by-cell and plane-by-plane charge features in Figs. 4(b) and 4(c) is within the corresponding estimated statistics errors. The *A*-site sums right neighboring the interface with a magnitude of slightly larger than unity [Fig. 2(c)] could be related to the background subtlety of the Nd- $N_{2,3}$ spectra across the interface, and the corresponding compositions given in the table were estimated by further referencing to the complementary chemical map exploiting the deep Nd- $M_{4,5}$ spectra (980–1010 eV), which exhibit a relatively robust background at those unit cells.

Unit-cell numbers	Unit-cell characters	Distance from the interface (Å)	Derived compositions
-5	NSMO	-20	$(Nd_{0.35}Sr_{0.65})(Mn_{0.97}Ti_{0.03})O_{3-\delta}^a$
-4	NSMO	-16	$(Nd_{0.35}Sr_{0.65})(Mn_{0.95}Ti_{0.05})O_{3-\delta}^a$
-3	NSMO	-12	$(Nd_{0.35}Sr_{0.65})(Mn_{0.9}Ti_{0.1})O_{3-\delta}^a$
-2	NSMO	-8	$(Nd_{0.33}Sr_{0.67})(Mn_{0.8}Ti_{0.2})O_{3-\delta}^a$
-1	NSMO	-4	$(Nd_{0.3}Sr_{0.7})(Mn_{0.54}Ti_{0.46})O_{3-\delta}^a$
0	Interface	0	$(Nd_{0.16}Sr_{0.84})(Mn_{0.22}Ti_{0.78})O_3$
1	STO	4	$(Sr_{0.955}Nd_{0.045})(Ti_{0.97}Mn_{0.03})O_3$
2	STO	8	$(Sr_{0.985}Nd_{0.015})TiO_3$
3	STO	12	SrTiO ₃
4	STO	16	SrTiO ₃
5	STO	20	SrTiO ₃

^aThe potential oxygen substoichiometry (δ) due to the possible presence of oxygen vacancies in these five unit cells is not included, otherwise half of the cell-by-cell charge values in Fig. 4(b).

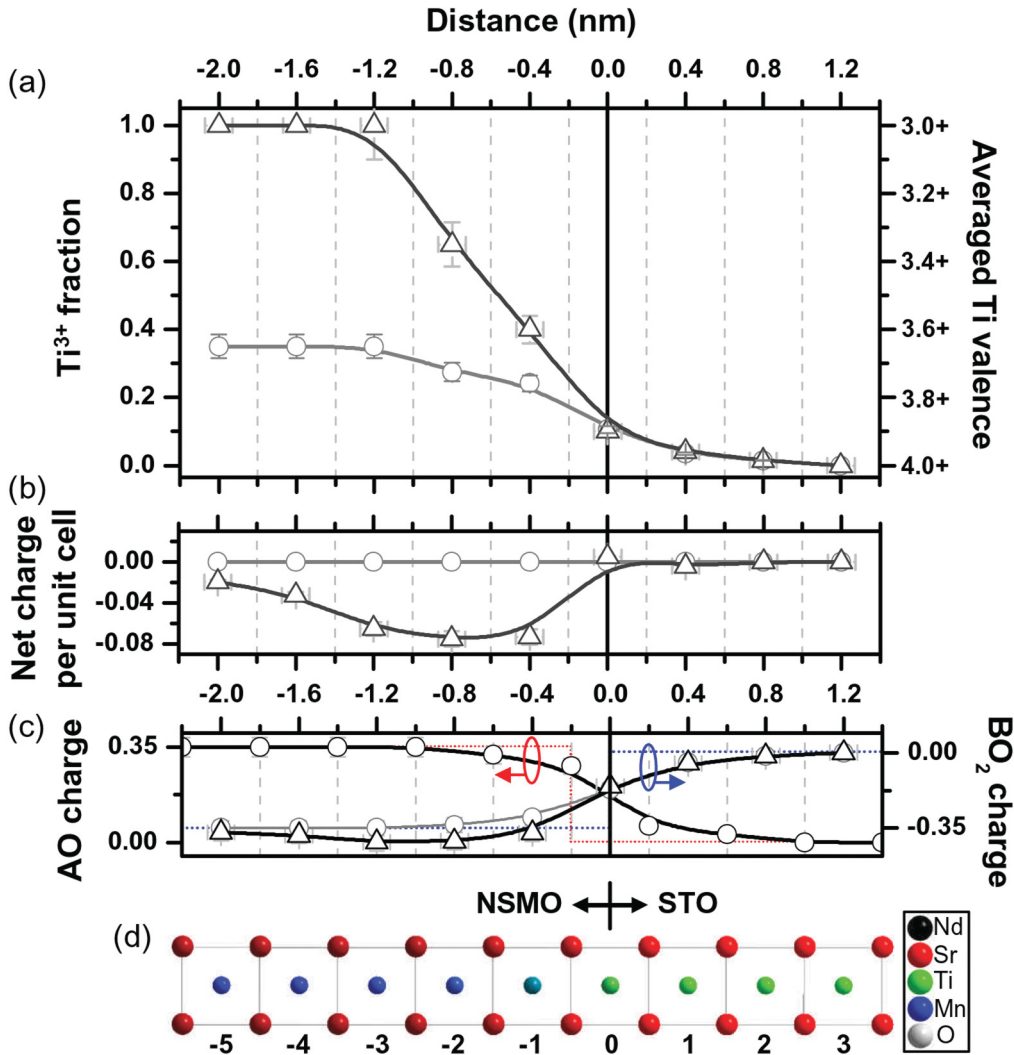


FIG. 4. (Color online) (a) The least-squares-fitted Ti^{3+} fractions, $Ti^{3+}/(Ti^{3+} + Ti^{4+})$, and thus-derived averaged Ti valences (triangles) in each $Ti-L_{2,3}$ spectrum [Fig. 3(a)]. Circles represent those evaluated using the charge-neutral formula of $(Nd_{1-x}Sr_x)(Mn_{1-y}Ti_y)O_3$. Vertical bars are estimated statistics errors of, at most, 10%. Horizontal bars are the probing mechanical instability of ~ 0.7 Å. (b) Unit-cell-by-unit-cell and (c) atomic-plane-by-atomic-plane charge characteristics (see text). Triangles (circles), represent experimental least-squares-fitted results (the charge-neutral formula estimations). Dotted lines in (c) are the primitive polar discontinuity. (d) The interfacial unit-cell scheme. The oxygen is ignored for simplicity.

In addition, the calculated Ti^{3+} fractions in Fig. 4(a) (circles) were obtained from the nominal charge neutrality of the general formula, $(Nd_{1-x}Sr_x)(Mn_{1-y}Ti_y)O_3$, and Fig. 4(d) depicts the interfacial unit cells with the atomic-site colors coded in accordance with the cell-specific compositions in Table I. From Fig. 4(c), it is notable that the primitive polar discontinuity at the NSMO/STO interface (red and blue dotted lines) is appreciably graded by the interdiffusion and the primitive electrostatic imbalance should not serve as an effective driving force for the associated charge transfer,^{6,23} which principally directs to the STO side.¹⁻⁴ A diminished charge density at the NSMO/STO interface would be expected, thus mediating an insulating interface with classically vanishing charge carriers.²⁰ The significant discrepancy between the nominally calculated (within the charge neutrality) and experimentally determined Ti^{3+} fractions in Fig. 4(a), however, indicates that a charge transfer inversely into NSMO does exist and in

Fig. 4(b) the corresponding length scale (~ 2 nm) and charge density [$\sim 3.75 \times 10^{13}/\text{cm}^2$; ~ 0.06 electron per unit cell in average; triangles, Fig. 4(b)] can be determined. In Fig. 4(b), it is noted that the charge density manifests a maximum at ~ 0.8 nm away from the interface. This charge-distribution pattern could be associated with the charge-screening property of the material²⁶ and requires further elaboration. At this insulating interface, the presence of such a significant two-dimensional electron density is, however, unexpected in the classical electrostatics.²⁰ More remarkably, the length scale of the electron density [Fig. 4(b)] is commensurate with the asymmetric Ti-interdiffusion length of also ~ 2 nm [Figs. 2(b) and 3(a)], suggesting a profound underlying consequence for the asymmetric Ti interdiffusion.

Indeed, NSMO manifests a work function of ~ 4.6 eV, close to ~ 4.5 – 4.6 eV of some insulating $(La_{1-x}Sr_x)MnO_3$.²⁶ Upon joining to the TiO_2 plane of STO with an associated

work function of ~ 4.2 eV,²⁷ the work-function difference of ~ 0.4 eV can potentially account for this inverse charge transfer into NSMO.²⁸ Notably, the Mn $3d$ band near the Fermi level becomes the electron reservoir^{19,26,28} [e.g., Fig. 6(a) below] and the observed averaged charge transfer of ~ 0.06 electron per unit cell [Fig. 4(b)] can be equivalent to performing an electron doping from the nominal Mn^{3.65+} to Mn^{3.59+}. In effect, the Mott-insulating NSMO is subject to an intricate electronic instability in the parent (Nd_{1-x}Sr_x)MnO₃ phase diagram within the range of Mn^{3.55+} ($x \sim 0.55$) and Mn^{3.75+} ($x \sim 0.75$).¹⁷⁻¹⁹ Upon an electronic deviation from Mn^{3.62+} ($x \sim 0.62$), a distinct ground-state transition from an insulator (Mn^{x+} > Mn^{3.62+}) to a metal (< Mn^{3.62+}) takes place, which also involves the transitions in the entangled lattice (tetragonal to orthorhombic unit cell), orbital [c -oriented $d_{3z^2-r^2}$ to ab -plane $d_{x^2-y^2}$, Fig. 1(a)], and spin (c - to ab -plane directed antiferromagnetic ordering) degrees of freedom.¹⁷⁻¹⁹ Taking this strongly correlated context of NSMO into account, the interface should be metallic upon the interfacial charge transfer due to its electron-doping essence from Mn^{3.65+} to Mn^{3.59+}. However, we observed both the persistent Mn^{3.65+} charge [Figs. 3(b) and 5] and insulating ground states [Figs. 1(b)] characteristic of NSMO,¹⁷⁻¹⁹ indicating that the conspicuous two-dimensional electron density in the interfacial NSMO could not be readily accommodated by a change of the Mn-charge state like the bulk. The presence of the interface appears to hamper the interplay among the various strongly correlated degrees of freedom generic to the parent phase

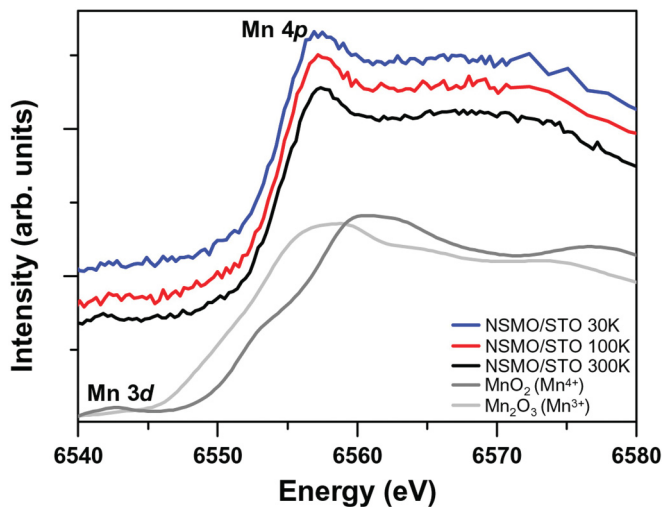


FIG. 5. (Color online) The Mn K -edge x-ray absorption near-edge structure spectra of the ~ 20 -nm-thick NSMO/STO heterostructure acquired at various temperatures and those of the reference oxides, Mn₂O₃ (Mn³⁺) and MnO₂ (Mn⁴⁺), at room temperature using synchrotron-radiation hard x rays. The principal spectral features arising from the excitations to the unoccupied $3d$ and $4p$ states are indicated, respectively. The spectral $4p$ -onset position of the NSMO at 300 K locates in between those of the reference oxides, pointing out a given mixed-valence character of the constituent Mn (i.e., nominally Mn^{3.65+}) at room temperature. This given Mn^{3.65+}-charge character is electronically stable at low temperatures as demonstrated by the practically constant line position and shape of the $4p$ onset at 100 and 30 K in the NSMO. The dipole-forbidden $3d$ -excitation onset in the NSMO is otherwise too weak to be further elaborated.

diagram. To accommodate this otherwise significant charge density, the Ti interdiffusion with its mixed-valence feasibility would be a fair compromise for NSMO, as derived from the observed mixed-valence Ti features in Fig. 3(a) and the comparable interdiffusion length to the length scale of the electron density [both ~ 2 nm, Figs. 3(a) and 4(b)].

The presence of Ti in the interfacial NSMO unit cells could promote an insulating character for the associated two-dimensional electron density considering the Ti substitution for Mn in metallic (La_{0.7}Sr_{0.3})MnO₃ bulks induces a transition into an insulating state due to a d -band narrowing by the Ti-induced structural distortion as a result of its larger ionic size.²⁹ To elaborate on this aspect, we have calculated the associated density of state (DOS) using approximately the STEM-EELS derived composition of unit cell - 2 (Table I). The results are shown in Fig. 6 along with the calculation for insulating Nd_{0.33}Sr_{0.67}MnO₃, which closely mimics the physical properties of current NSMO (Refs. 18,19) and manifests a composition that can be practically considered in a reasonably sized supercell ($\sqrt{2} \times \sqrt{2} \times 3$). This latter supercell-size argument also accounts for the composition considered in Fig. 6(b), close to that of unit cell - 2. Indeed, Fig. 6(b) suggests an insulating feature of this Ti-containing unit cell with a d -band narrowing of ~ 0.2 eV [see the $d_{3z^2-r^2}$ -orbital DOS of spin-up Mn compared to that of Nd_{0.33}Sr_{0.67}MnO₃ in Fig. 6(a)]. This narrowing is induced by an associated BO_6 -octahedral distortion through the Ti-mediated elongation of the in-plane $B-O$ bond by 0.03–0.05 Å. The out-of-plane $B-O$ bond is otherwise little affected. Although a thorough theoretical understanding of the NSMO/STO interface requires the unit-cell-by-unit-cell interfacial calculations incorporating each respective composition in Table I, such calculations would be computationally enormous and represent a separate work on its own. Indeed, the results in Fig. 6 can capture the insulating essence for the interfacial NSMO unit cells. The elaborately determined compositions of the interfacial STO unit cells, 1 and 2 (Table I), also shed light on their insulating features, since these unit cells could be regarded as (Sr_{1-x}Nd_x)TiO₃ with effectively $x < 5\%$ and established insulating characteristics.³⁰ In addition, the interdiffusion-induced disorder can also be a factor in the localization of a two-dimensional electron density,³¹ and the potential contribution of a plausibly enhanced insulating property of NSMO and/or neighboring compounds in the phase diagram at the currently reduced two-dimensional scale might also exist. Accordingly, the two-dimensional charge density in the interfacial NSMO unit cells would tend to be localized,³¹ resulting in the insulating interface. It should be also mentioned that the charge density in NSMO [Fig. 4(b)] might be accompanied with oxygen vacancies taking into account the electron-donor character of the vacancies.^{6,10-12} Nevertheless, the insulating two-dimensional electron density in NSMO should not be driven by oxygen vacancies, since adequate oxidized atmospheres upon the heterostructure growth and postannealing have been applied for filling oxygen defects.⁶ The possible pairing up of the insulating two-dimensional electron density in NSMO and oxygen vacancies appears to be counterintuitive, considering the electron-donor oxygen vacancies are conventionally entangled with a metallic property,^{6,10-12} and remains to be profoundly tackled.

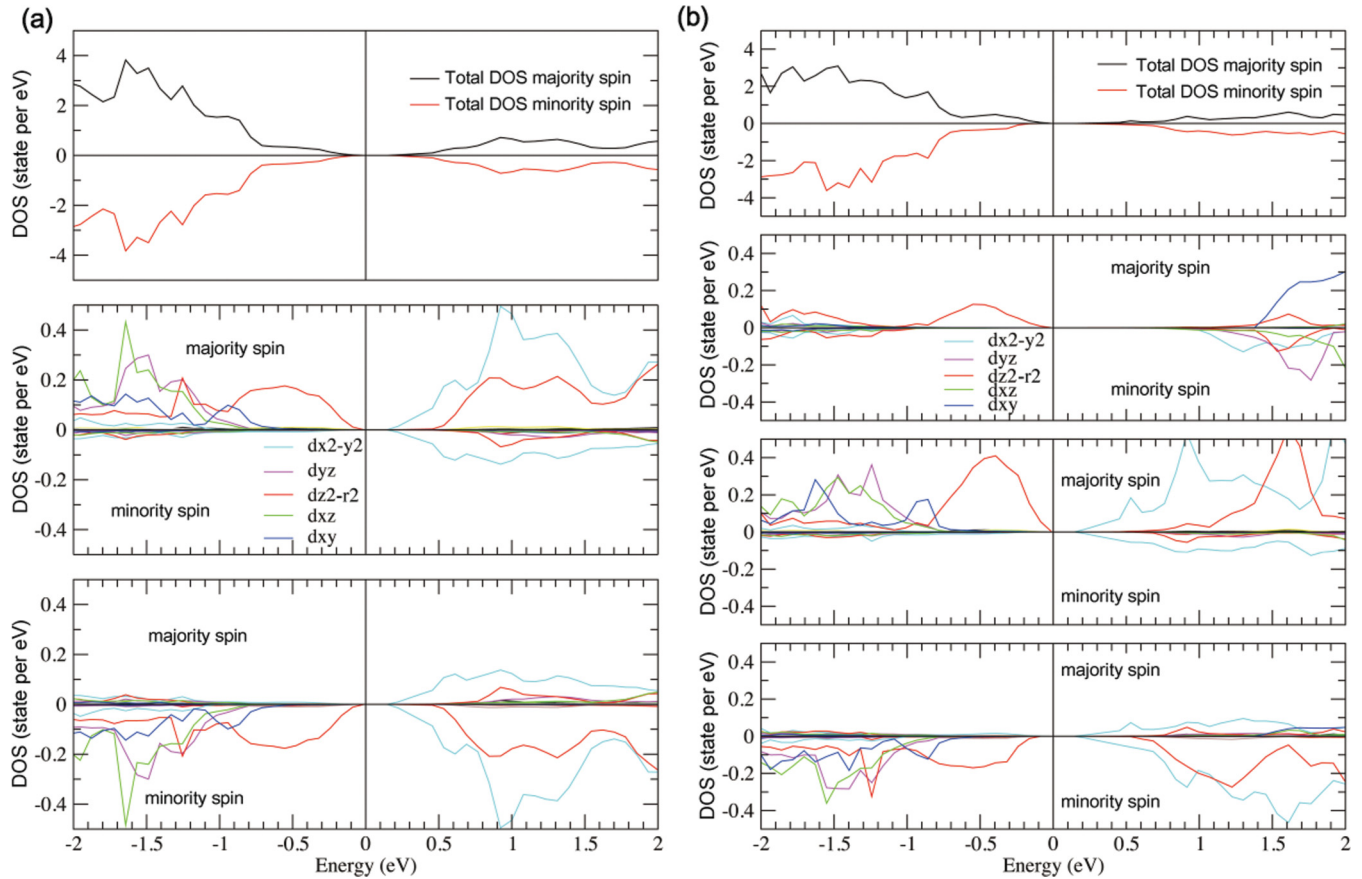


FIG. 6. (Color online) The calculated DOS of (a) $\text{Nd}_{0.33}\text{Sr}_{0.67}\text{MnO}_3$ and (b) $\text{Nd}_{0.33}\text{Sr}_{0.67}(\text{Mn}_{0.83}\text{Ti}_{0.17})\text{O}_3$ unit cells taking into account the c -oriented (so-called C -type) antiferromagnetic ordering of nominal NSMO (Refs. 18,19). Top to bottom in (a), the total DOS, the orbital-decomposed DOS of spin-up Mn, and those of spin-down Mn. The experimentally determined band gap of ~ 0.1 eV for NSMO is acceptably reproduced herein (~ 0.2 eV) (Ref. 19). Top to bottom in (b), the total DOS, the orbital-decomposed DOS of spin-up Ti, those of spin-up Mn, and those of spin-down Mn. The theoretically estimated band gap of ~ 0.2 eV in (a) is nearly unchanged, and the doped Ti displays the spin-up and $d_{3z^2-r^2}$ -orbital features, characteristic of Mn (see the second and third panels from the top). Intriguingly, the $d_{3z^2-r^2}$ bandwidth of the spin-up Mn is reduced by ~ 0.2 eV as a result of the Ti-induced structural distortion, enhancing an electronic localization of the correlated state. By contrast, the bandwidth of the spin-down Mn is not visibly affected by the spin-up Ti incorporation, as shown in the bottom panels of (a) and (b). For simplicity, $d_{3z^2-r^2}$ is denoted as $d_{z^2-r^2}$ in the figure. The calculations were performed in the VASP package using the full-potential augmented wave method within the generalized gradient approximation (GGA) plus an on-site Hubbard repulsion (U) of 5 eV. The respective geometries of the supercells studied were optimized with the residual atomic force of less than $0.01/\text{eV}/\text{\AA}$.

IV. CONCLUSION

In summary, the insulating NSMO/STO interface is not expected to display a residual charge density from the viewpoints of both the classical electrostatics²⁰ and the graded polar discontinuity.^{6,23} Using atomic-plane-by-atomic-plane, unit-cell-by-unit-cell characterizations, the existence of a localized two-dimensional electron density therein was, however, unambiguously resolved and the corresponding length scale (~ 2 nm) and charge density (on the order of $\sim 10^{13}/\text{cm}^2$) have been determined. These results, though presently only for NSMO/STO, could extend the current understanding in an insulating oxide interface between two insulators.^{14,20} Furthermore, the observation of a localized two-dimensional electron density in NSMO is at odds with the classical metallic 2DEG in STO for LAO/STO and LTO/STO,¹⁻¹³ whereas the associated length scale and charge density are surprisingly close to those of the 2DEG counterpart.^{1,2,4,10,21,22}

This notable similarity would be an intriguing subject in the future and our plane-specific, cell-specific stoichiometry and charge characterizations can be of interest to LAO/STO and LTO/STO for ultimately resolving the corresponding effective polar discontinuity.⁵⁻⁹ A thorough STEM-EELS characterization of the conductive LAO/STO interface is indeed under way. Otherwise explorations could be a systematic study of an electron density on either side of the interface through various strongly correlated oxides (metals or insulators) and the interplay between the electron density and the various physical degrees of freedom of the given materials, such as the metal/insulator junction of $(\text{La}_{0.7}\text{Sr}_{0.3})\text{MnO}_3/\text{STO}$ with a yet unexplained asymmetric Ti interdiffusion into the metal side.^{15,32} Indeed, in NSMO the Ti-induced distortion related to the localized electron density (Fig. 6) could be in a subtle balance with the in-plane tensile strain by STO. This conjugated condition seemingly suggests a possible strain

engineering on the electronic localization of the electron density by an interfacial mismatch optimization²⁵ or an applied force parallel/perpendicular to the interface analogous to a piezoelectric manipulation, potentially casting a technological aspect on the exploitation of this insulating interface. Our work does point to profound opportunities in strongly correlated oxide interfaces, in which the interfacial characteristics could be more difficult to predict.

ACKNOWLEDGMENTS

We thank Professor C. Colliex, Professor H. Y. Hwang, and Dr. T. Feder for enlightening discussions on the results and the technical assistance of Dr. S.-S. Li, Dr. C. T. Wu, Dr. J. M. Chen, Professor C. H. Du, Dr. F. C. Chou, and Dr. C.-H. Hsu. This work was supported by National Science Council of Taiwan, National Taiwan University, and Academia Sinica Taiwan.

*Corresponding author: chumingwen@ntu.edu.tw

¹J. Mannhart and D. G. Schlom, *Science* **327**, 1607 (2010).

²H. Y. Hwang, Y. Iwasa, M. Kawasaki, B. Keimer, N. Nagaosa, and Y. Tokura, *Nat. Mater.* **11**, 103 (2012).

³A. Ohtomo and H. Y. Hwang, *Nature* **427**, 423 (2004).

⁴J. Biscaras, N. Bergeal, A. Kushwaha, T. Wolf, A. Rastogi, R. C. Budhani, and J. Lesueur, *Nat. Commun.* **1**, 89 (2010).

⁵A. Ohtomo, D. A. Muller, J. L. Grazul, and H. Y. Hwang, *Nature* **419**, 378 (2002).

⁶N. Nakagawa, H. Y. Hwang, and D. A. Muller, *Nat. Mater.* **5**, 204 (2006).

⁷P. R. Willmott, S. A. Pauli, R. Herger, C. M. Schlepütz, D. Martoccia, B. D. Patterson, B. Delley, R. Clarke, D. Kumah, C. Cionca, and Y. Yacoby, *Phys. Rev. Lett.* **99**, 155502 (2007).

⁸S. A. Pauli, S. J. Leake, B. Delley, M. Björck, C. W. Schneider, C. M. Schlepütz, D. Martoccia, S. Paetel, J. Mannhart, and P. R. Willmott, *Phys. Rev. Lett.* **106**, 036101 (2011).

⁹A. S. Kalabukhov, Yu. A. Boikov, I. T. Serenkov, V. I. Sakharov, V. N. Popok, R. Gunnarsson, J. Börjesson, N. Ljustina, E. Olsson, D. Winkler, and T. Claeson, *Phys. Rev. Lett.* **103**, 146101 (2009).

¹⁰M. Basletic, J.-L. Maurice, C. Carrétéro, G. Herranz, O. Copie, M. Bibes, E. Jacquet, K. Bouzouane, S. Fusil, and A. Barthélémy, *Nat. Mater.* **7**, 621 (2008).

¹¹A. Brinkman, M. Huijben, M. van Zalk, J. Huijben, U. Zeitler, J. C. Maan, W. G. van der Wiel, G. Rijnders, D. H. A. Blank, and H. Hilgenkamp, *Nat. Mater.* **6**, 493 (2007).

¹²G. Herranz, M. Basletic, M. Bibes, C. Carrétéro, E. Tafra, E. Jacquet, K. Bouzouane, C. Deranlot, A. Hamzić, J. M. Broto, A. Barthélémy, and A. Fert, *Phys. Rev. Lett.* **98**, 216803 (2007).

¹³A. J. Millis, *Nat. Phys.* **7**, 749 (2011).

¹⁴S. A. Chambers, L. Qiao, T. C. Droubay, T. C. Kaspar, B. W. Arey, and P. V. Sushko, *Phys. Rev. Lett.* **107**, 206802 (2011).

¹⁵D. A. Muller, L. Fitting Kourkoutis, M. Murfitt, J. H. Song, H. Y. Hwang, J. Silcox, N. Dellby, and O. L. Krivanek, *Science* **319**, 1073 (2008).

¹⁶M.-W. Chu, S. C. Liou, C. P. Chang, F.-S. Choa, and C. H. Chen, *Phys. Rev. Lett.* **104**, 196101 (2010).

¹⁷Sh. Xu, Y. Moritomo, A. Machida, K. Ohoyama, K. Kato, and A. Nakamura, *Phys. Rev. B* **66**, 024420 (2002).

¹⁸R. Kajimoto, H. Yoshizawa, H. Kawano, H. Kuwahara, Y. Tokura, K. Ohoyama, and M. Ohashi, *Phys. Rev. B* **60**, 9506 (1999).

¹⁹K. Tobe, T. Kimura, and Y. Tokura, *Phys. Rev. B* **67**, 140402(R) (2003).

²⁰M. Stengel and D. Vanderbilt, *Phys. Rev. B* **80**, 241103(R) (2009).

²¹M. Huijben, G. Rijnders, D. H. Blank, S. Bals, S. van Aert, J. Verbeeck, G. van Tendeloo, A. Brinkman, and H. Hilgenkamp, *Nat. Mater.* **5**, 556 (2006).

²²M. Sing, G. Berner, K. Goss, A. Müller, A. Ruff, A. Wetscherek, S. Thiel, J. Mannhart, S. A. Pauli, C. W. Schneider, P. R. Willmott, M. Gorgoi, F. Schäfers, and R. Claessen, *Phys. Rev. Lett.* **102**, 176805 (2009).

²³W. A. Harrison, E. A. Kraut, J. R. Waldrop, and R. W. Grant, *Phys. Rev. B* **18**, 4402 (1978).

²⁴M. Abbate, F. M. F. de Groot, J. C. Fuggle, A. Fujimori, Y. Tokura, Y. Fujishima, O. Strebler, M. Domke, G. Kaindl, J. van Elp, B. T. Thole, G. A. Sawatzky, M. Sacchi, and N. Tsuda, *Phys. Rev. B* **44**, 5419 (1991).

²⁵H. W. Jang, D. A. Felker, C. W. Bark, Y. Wang, M. K. Niranjan, C. T. Nelson, Y. Zhang, D. Su, C. M. Folkman, S. H. Baek, S. Lee, K. Janicka, Y. Zhu, X. Q. Pan, D. D. Fong, E. Y. Tsymbal, M. S. Rzchowski, and C. B. Eom, *Science* **331**, 886 (2011).

²⁶S. Yunoki, A. Moreo, E. Dagotto, S. Okamoto, S. S. Kancharla, and A. Fujimori, *Phys. Rev. B* **76**, 064532 (2007).

²⁷T. Susaki, A. Makishima, and H. Hosono, *Phys. Rev. B* **84**, 115456 (2011).

²⁸E. Dagotto, *Science* **318**, 1076 (2007).

²⁹M. S. Kim, J. B. Yang, Q. Cai, X. D. Zhou, W. J. James, W. B. Yelon, P. E. Parris, D. Buddhikot, and S. K. Malik, *Phys. Rev. B* **71**, 014433 (2005).

³⁰S. W. Robey, V. E. Henrich, C. Eylem, and B. W. Eichhorn, *Phys. Rev. B* **52**, 2395 (1995).

³¹Z. S. Popović, S. Satpathy, and R. M. Martin, *Phys. Rev. Lett.* **101**, 256801 (2008).

³²Y. Hikita, M. Nishikawa, T. Yajima, and H. Y. Hwang, *Phys. Rev. B* **79**, 073101 (2009).